A New Pan-Sharpening Method Using a Compressed Sensing Technique

Shutao Li, *Member, IEEE*, and Bin Yang

***Abstract*—This paper addresses the remote sensing image pan-sharpening problem from the perspective of compressed sensing (CS) theory which ensures that with the sparsity regularization, a compressible signal can be correctly recovered from the global linear sampled data. First, the degradation model from a high- to low-resolution multispectral (MS) image and high-resolution panchromatic (PAN) image is constructed as a linear sampling process which is formulated as a matrix. Then, the model matrix is considered as the measurement matrix in CS, so pan-sharpening is converted into signal restoration problem with sparsity regularization. Finally, the basis pursuit (BP) algorithm is used to resolve the restoration problem, which can recover the high-resolution MS image effectively. The QuickBird and IKONOS satellite images are used to test the proposed method. The experimental results show that the proposed method can well preserve spectral and spatial details of the source images. The pan-sharpened high-resolution MS image by the proposed method is competitive or even superior to those images fused by other well-known methods.**

***Index Terms*—Compressed sensing, image fusion, multispectral (MS) image, panchromatic (PAN) image, remote sensing, sparse representation.**

I. Introduction

OPTICAL remote sensors in satellites can provide images about the surface of the Earth which are valuable for environmental monitoring, land-cover classification, weather forecasting, etc. Practically, most optical Earth observation satellites, such as QuickBird and IKONOS, provide image data with spectral and spatial information separately, such as low-resolution multispectral (MS) images and high-resolution panchromatic (PAN) image. In order to benefit from both spectral and spatial information, these two kinds of images can be fused to get one high-spectral- and high-spatial-resolution remote sensing image [1]. The fusing process, classically referred as pan-sharpening technique, has become a key preprocessing step in many remote sensing applications [2].

Various methods have been proposed for pan-sharpening, which usually consider physics of the remote sensing process and make some assumptions on the original PAN and MS images [3]–[7]. The most classical methods are projection–substitution-based which assume that the PAN image is equivalent to the structural component of the MS images when projected the MS images into a new space. The most famous projection–substitution methods include the intensity hue saturation (IHS) [8], [9], the principal component analysis [10], the Gram–Schmidt (GS) transform [11] based methods, and so on.

In recent years, the methods based on the ARSIS concept have been popular which assume that the missing spatial information in the MS images can be obtained from the high frequencies of the PAN image [12], [13]. In [2], Thomas *et al.* showed that this category method prevents from introducing spectral distortion into fused products in some degree. Thus, it offers a reliable framework for further developments. The multiresolution transforms, such as discrete wavelet transform (DWT) [6], "à trous" wavelet transform (ATWT) [14], contourlets [15], and support value transform [16], are usually used to extract the high frequencies of the PAN image. The ATWT allows an image to be decomposed into nearly disjointed bandpass changes in spatial frequency domain, which makes it particularly suitable for remote image fusion. An ATWT-based method with the additive wavelet luminance proportional (AWLP) model was proposed in [17]. The AWLP model injects high-pass details proportionally to low-pass MS components, and improves the spectral quality of fused image.

Nevertheless, the high frequencies extracted from the PAN image are not exactly equivalent to those of the MS images. So adjusting those high frequencies, called the interband structure model (IBSM) [13], is needed before they are injected into the MS images. One of the famous IBSMs is the context-based injection model [18]. The undecimated DWT or the generalized Laplacian pyramid is used to extract the high-frequency details of the PAN image. Garzelli and Nencini proposed the ATWT-based method with context-based decision (CBD) injection model in [19]. The experimental results showed that the CBD model yields better results than those traditional methods. In addition, Garzelli and Nencini applied the genetic algorithm [20] to optimize the injection model of the ATWT-based method by maximizing the quality index of the fused product, and the pan-sharpening results are obviously improved.

Also, as a popular idea, the inverse-problem-based methods are used to restore the original high-resolution MS image from its degraded versions, i.e., the PAN and MS images [21], [22]. Because much information is lost in the degrading process, this is an ill-posed inverse problem and the solution is not unique. This means that according to the degrading process, many different high-resolution MS images can produce the same high-resolution PAN and low-resolution MS images. Thus, various

Manuscript received November 27, 2009; revised April 5, 2010 and July 2, 2010; accepted August 5, 2010. Date of publication October 11, 2010; date of current version January 21, 2011. This work was supported in part by the National Natural Science Foundation of China (No. 60871096), the Ph.D. Programs Foundation of Ministry of Education of China (No.200805320006), the Key Project of Chinese Ministry of Education (2009-120), and the Open Projects Program of National Laboratory of Pattern Recognition.

The authors are with the College of Electrical and Information Engineering, Hunan University, Changsha 410082, China (e-mail: shutao_li@yahoo.com.cn; yangbin01420@163.com).

Color versions of one or more of the figures in this paper are available online at http://ieeexplore.ieee.org.

Digital Object Identifier 10.1109/TGRS.2010.2067219

regularization-based methods have been proposed to resolve the ill-posed inverse problem [23], [24]. In [23], the pan-sharpening process is modeled as restoring the high-resolution MS images aided by the PAN image. The fused results can preserve spectral characteristics of the true MS images as well as high spatial resolution of the source PAN image. The regularization and iterative optimal method was proposed in [24], in which the fused result is obtained through optimizing an image quality index. The Bayesian method is an important tool to resolve ill-posed inverse problems [25]–[27]. Within the Bayesian framework, the fused image is extracted from the Bayesian posterior distribution in which the prior knowledge and artificial constraints on the fusion results are incorporated. Joshi and Jalobeanu modeled the pan-sharpening problem as separate inhomogeneous Gaussian Markov random fields and applied a maximum *a posteriori* estimation to obtain the fused image for each MS band [27]. The experiments on both synthetic data and the QuickBird satellite images demonstrate its effectiveness. However, its performance would degrade if there are not enough training images.

Recently, Donoho and Candès *et al.* proposed a new sampling theory, compressed sensing (CS) theory, for data acquisition [28], [29]. The CS theory can recover an unknown sparse signal from a small set of linear projections, which has been applied in many image processing applications [30]–[34]. The key point of CS theory is the sparsity regularization which refers to the nature of the natural signals [28]. It is very suitable to resolve the inverse problem of compressible signals/images. With the perspective of compressed sensing, this paper proposes a novel pan-sharpening method with sparsity regularization. We formulate the remote sensing imaging formation model as linear transform corresponding to the measurement matrix in the CS theory and the high-resolution PAN and low-resolution MS images are referred as measurements. Thus, based on the sparsity regularization, the high-resolution MS images can be recovered precisely.

The rest of this paper is organized into five sections. In Section II, the sparsity representation and the CS theory are briefly introduced. In Section III, we give the model of the high-resolution PAN image and the low-resolution MS images from the high-resolution MS images. Then, the fusion scheme based on the CS theory is proposed. Numerical experiments and discussions are presented in Section IV. Conclusions together with some suggestions about the future work are given in Section V.

II. Sparse Representation and Compressed Sensing

The development of image processing in the past several decades reveals that a reliable image model is very important. In fact, natural images tend to be sparse in some image bases' space [30]. This brings us to the sparse and redundant representation model of image.

Consider a family of signals $\{\boldsymbol{x}_i, i = 1, 2, \ldots, g\}$, $\boldsymbol{x}_i \in \mathbf{R}^n$. Specially, in this paper, each such signal is assumed to be a $\sqrt{n} \times \sqrt{n}$ image patch, obtained by lexicographically stacking the pixel values. Sparse representation theory supposes the existence of a matrix $\mathbf{D} \in \mathbf{R}^{n \times T}$, $n \ll T$, each column of which corresponds to a possible image (lexicographically stacking the pixel values as a vector). These possible images are referred to as atomic images, and the matrix $\mathbf{D}$ as a dictionary of the atomic images. Thus, an image signal $\boldsymbol{x}$ can be represented as $\boldsymbol{x} = \mathbf{D}\boldsymbol{\alpha}$. For overcomplete $\mathbf{D}$ $(n \ll T)$, there are many possible $\boldsymbol{\alpha}$ satisfying $\boldsymbol{x} = \mathbf{D}\boldsymbol{\alpha}$. Our aim is to find the $\boldsymbol{\alpha}$ with the fewest nonzero elements. Thus, the $\boldsymbol{\alpha}$ is called the sparse representation of $\boldsymbol{x}$ with dictionary $\mathbf{D}$. Formally, this problem can be obtained by solving the following optimization problem:

$$\hat{\boldsymbol{\alpha}} = \arg\min \|\boldsymbol{\alpha}\|_0 \quad s.t. \|\mathbf{D}\boldsymbol{\alpha} - \boldsymbol{x}\|_2^2 = 0 \tag{1}$$

where $\|\boldsymbol{\alpha}\|_0$ denotes the number of nonzero components in $\boldsymbol{\alpha}$.

In practice, because of various restrictions, we cannot get $\boldsymbol{x}$ directly; instead, only a small set of measurements $\boldsymbol{y}$ of $\boldsymbol{x}$ is observed. The observation $\boldsymbol{y}$ can be represented as

$$\boldsymbol{y} = \mathbf{L}\boldsymbol{x} \tag{2}$$

where $\mathbf{L} \in \mathbf{R}^{k \times n}$ with $k < n$. (2) is interpreted as the encode process of the CS theory, where $\mathbf{L}$ is a CS measurement matrix. The CS theory ensures that under sparsity regularization [29], the signal $\boldsymbol{x}$ can be correctly recovered from the observation $\boldsymbol{y}$ by

$$\min \|\boldsymbol{\alpha}\|_0 \quad s.t. \|\boldsymbol{y} - \boldsymbol{\Phi}\boldsymbol{\alpha}\|_2^2 \leq \boldsymbol{\varepsilon} \tag{3}$$

where $\boldsymbol{\Phi} = \mathbf{LD}$, ε is the reconstruction error which depends on noise level of source image, and $\boldsymbol{x} = \mathbf{D}\boldsymbol{\alpha}$. The effectiveness of sparsity as a prior for regularizing the ill-posed problem has been validated by many literatures [30]–[34]. In this paper, we propose one remote sensing image fusion method from the perspective of compressed sensing. The high-resolution PAN and low-resolution MS images are referred as the measurements $\boldsymbol{y}$. The matrix $\mathbf{L}$ is constructed by the model from the high-resolution MS images to the high-resolution PAN and low-resolution MS images. Thus, the sparse representation $\boldsymbol{\alpha}$ of the high-resolution MS images corresponding to dictionary $\mathbf{D}$ can be recovered from measurements $\boldsymbol{y}$ according to the sparsity regularization of (3), and the high-resolution MS images are constructed by $\boldsymbol{x} = \mathbf{D}\boldsymbol{\alpha}$.

However, because $\|\boldsymbol{\alpha}\|_0$ is combinatorial, the above optimization is an NP-hard problem [30]. In fact, when the coefficients are sufficiently sparse, this problem can be replaced with minimizing the l_1-norm problem

$$\min \|\boldsymbol{\alpha}\|_1 \quad s.t. \|\boldsymbol{y} - \boldsymbol{\Phi}\boldsymbol{\alpha}\|_2^2 \leq \boldsymbol{\varepsilon}. \tag{4}$$

The proof from (3) to (4) can be found in [35]. The l_1-norm problem (4) can be efficiently resolved by the basis pursuit (BP) method [36]. In the BP method, (4) is converted to the standard linear program formed as

$$\min \boldsymbol{c}^T\boldsymbol{\theta} \quad s.t. \boldsymbol{A}\boldsymbol{\theta} = \boldsymbol{b}, \boldsymbol{\theta} \geq 0 \tag{5}$$

where $\boldsymbol{\theta} = (\boldsymbol{\alpha}^+; \boldsymbol{\alpha}^-)$; $\boldsymbol{c} = (\mathbf{1}; \mathbf{1})$; $A = (\boldsymbol{\Phi}, -\boldsymbol{\Phi})$; $\boldsymbol{b} = \boldsymbol{y}$. Then, the sparse representation in (4) can be obtained by $\hat{\boldsymbol{\alpha}} = \boldsymbol{\alpha}^+ - \boldsymbol{\alpha}^-$. The sharpened high-resolution MS image patch is obtained by $\hat{\boldsymbol{x}} = \mathbf{D}\hat{\boldsymbol{\alpha}}$.

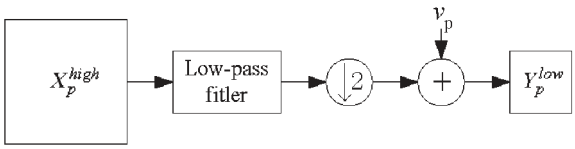

Fig. 1. Relationship between a single low-resolution MS band and its corresponding high-resolution version (↓ 2 means the decimation).

III. Proposed Image Fusion Scheme

A. Image Formation Model

Remote sensing physics should be carefully considered while designing the pan-sharpening process. Let $\boldsymbol{X}_p^{high}$ and $\boldsymbol{Y}_p^{low}$, $p = 1, \ldots, P$, represent the pth band of the high-resolution and low-resolution MS images, respectively, where P denotes the number of bands of the MS images. The observed low-resolution MS images are modeled as decimated and noisy versions of the corresponding high-resolution MS images, as shown in Fig. 1.

In fact, intensity of the low-resolution image is due to integration of light intensity that falls on the charge-coupled device sensor array of suitable area compared to the desired the high-resolution images [23], so the low-resolution intensity can be seen as neighborhood pixels' average of the high-resolution intensities corrupted with additive noise. The relationship between $\boldsymbol{X}_p^{high}$ and $\boldsymbol{Y}_p^{low}$ is written as

$$\boldsymbol{Y}_p^{low} = \mathbf{M}\boldsymbol{X}_p^{high} + \boldsymbol{v}_p \tag{6}$$

where $\mathbf{M}$ is the decimation matrix and $\boldsymbol{v}_p$ is the noise vector.

In fact, the PAN image usually covers a broad range of the wavelength spectrum; whereas, one MS band covers only a narrow spectral range. Moreover, the range of wavelength spectrum of the PAN modality is usually overlapped or partly overlapped with those of the MS bands. This overlapping characteristic motivates us making the assumption that the PAN image is approximately written as a linear combination of the original MS images

$$\boldsymbol{Y}^{PAN} = \sum_p \boldsymbol{w}_p \boldsymbol{X}_p^{high} + \boldsymbol{v}_p \tag{7}$$

where w_p is the weight and $\boldsymbol{v}_p$ is the additive zero-mean Gaussian noise [29]. However, we should note that the linear relationship between the PAN and the MS image is only approximated by the linear model because of the complexity of physics, atmospheric dispersion, and so on.

We consider a pan-sharpening case with four spectral bands: 1) Red (R); 2) green (G); 3) blue (B); 4) and near infrared (NIR), and the decimation factor from high to low spatial resolution is four. Fig. 2 shows the remote sensing image formation model, representing the relationship between the available low-resolution MS images and its high-resolution versions. Let $\boldsymbol{x} = (x_{1,1}, \ldots, x_{1,16}, \ldots, x_{4,1}, \ldots, x_{4,16})^T$ represent the lexicographically ordered high-spatial-resolution MS image patch and $\boldsymbol{y}_{MS} = (y_1, y_2, y_3, y_4)^T$ is the vector consisting of the pixels from the low-resolution MS images shown in Fig. 2. Then, we can write

$$\boldsymbol{y}_{MS} = \mathbf{M}_1\boldsymbol{x} + \boldsymbol{v}_1 \tag{8}$$

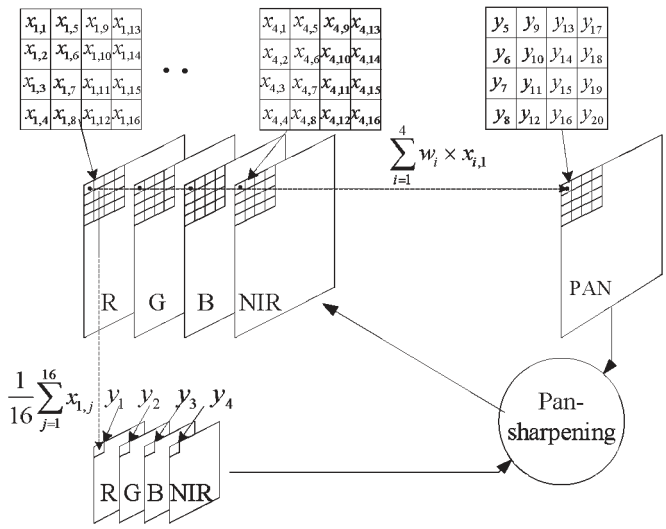

Fig. 2. Remote sensing image formation model.

where $\mathbf{M}_1$ is the decimation matrix of size 4×64 and $\boldsymbol{v}_1$ is the 4×1 zero-mean Gaussian noise vector. The $\mathbf{M}_1$ matrix can be written as $\mathbf{M}_1 = (1/16) \cdot \mathbf{I} \otimes \mathbf{1}^{\mathbf{T}}$, where $\mathbf{I} \in \mathbf{R}^{4\times4}$ is an identity matrix, and $\mathbf{1}$ is a 16×1 vector with all entries equaling to one.

Let $\boldsymbol{y}_{PAN} = (y_5, \ldots, y_{20})^T$ as the corresponding lexicographically ordered high-resolution PAN image patch, then we can write

$$\boldsymbol{y}_{PAN} = \mathbf{M}_2\boldsymbol{x} + \boldsymbol{v}_2 \tag{9}$$

where $\mathbf{M}_2 = (w_1\mathbf{I}, \quad w_2\mathbf{I}, \quad w_3\mathbf{I}, \quad w_4\mathbf{I})$, and $\mathbf{I} \in \mathbf{R}^{16\times16}$ is an identity matrix. The $\boldsymbol{v}_2$ is the additive zero-mean Gaussian noise vector. We assume that $\boldsymbol{v}_1$ and $\boldsymbol{v}_2$ have the same standard deviation σ. Then, combining (8) and (9), we get

$$\boldsymbol{y} = \mathbf{M}\boldsymbol{x} + \boldsymbol{v} \tag{10}$$

where $y = \binom{\boldsymbol{y}_{MS}}{\boldsymbol{y}_{PAN}}$ and $\mathbf{M} = \binom{\mathbf{M}_1}{\mathbf{M}_2}$.

The goal of image fusion is to recover $\boldsymbol{x}$ from $\boldsymbol{y}$. As shown in Section II, if signal is compressible by a sparsity transform, the CS theory ensures that the original signal can be accurately reconstructed from a small set of incomplete measurements. Thus, the signal recovering problem of (10) can be formulated as a minimization problem with sparsity constraints

$$\hat{\boldsymbol{\alpha}} = \arg\min \|\boldsymbol{\alpha}\|_0 \quad s.t. \|\boldsymbol{y} - \boldsymbol{\Phi\alpha}\|_2^2 \le \boldsymbol{\varepsilon} \tag{11}$$

where $\boldsymbol{\Phi} = \mathbf{MD}$, $\mathbf{D} = (d_1, d_2, \ldots, d_K)$ is a dictionary and $\boldsymbol{x} = \mathbf{D}\boldsymbol{\alpha}$ which explains $\boldsymbol{x}$ as a linear combination of columns from D. The vector $\hat{\boldsymbol{\alpha}}$ is very sparse. Finally, the estimated $\hat{\boldsymbol{x}}$ can be obtained by $\hat{\boldsymbol{x}} = \mathbf{D}\hat{\boldsymbol{\alpha}}$. In this paper, we assume that the source images are only contaminated by the additive zero-mean Gaussian noise. Thus, the parameter ε can be set by $\varepsilon = n(C\sigma)^2$, where n is the length of $\boldsymbol{y}$, C is a constant [31]. The noise level is estimated by user according to real satellite optical imaging system, and the constant C can be set by the generalized Rayleigh law as described in [31]. In the following experiments, the constant C is set to 1.15 for 8×8 image patch [32]. We can see that (11) is the same as (3) mentioned in

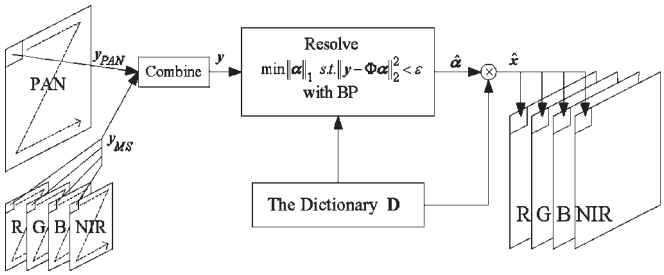

Fig. 3. Proposed fusion scheme.

Section II. Thus, this problem can be easily resolved by the BP method [36].

In addition, we should note that (11) is operated on $4 \times 4 \times 4$ image patch in the high-resolution MS images corresponding to 4×4 image patch in the PAN image and one pixel in each band of the MS images. However, such small patch contains little texture and structure information. On the other hand, a large patch captures local texture well but lacks generalization capability, and involves high computational complexity. In this paper, we set the size of image patch in the high-resolution MS images as $8 \times 8 \times 4$, corresponding to 8×8 image patch in the PAN image and $2 \times 2 \times 4$ patch in the low-resolution MS images, which appears to be a good tradeoff. Thus, the matrix $\mathbf{M}_1$ in (8) is constructed as $(1/16) \cdot \mathbf{I}_{8\times 8} \otimes (\mathbf{1}^{\mathrm{T}} \otimes (\mathbf{I}_{2\times 2} \otimes \mathbf{1}^{\mathrm{T}}))$, where $\mathbf{I}_{N\times N}$ is a $N \times N$ identity matrix and $\mathbf{1}$ is a 4×1 vector with all entries equal to one. The matrix $\mathbf{M}_2$ in (9) is constructed as $(w_1\mathbf{I} \quad w_2\mathbf{I} \quad w_3\mathbf{I} \quad w_4\mathbf{I})$ where $\mathbf{I} \in \mathbf{R}^{64\times 64}$ is an identity matrix.

The proposed pan-sharpening scheme is illustrated in Fig. 3. As shown in Fig. 3, all the patches of the PAN and MS images are processed in raster-scan order, from left-top to right-bottom with step of four pixels in the PAN image and one pixel in the MS images. First, according to Fig. 3, the PAN patch $\boldsymbol{y}_{PAN}$ is combined with the MS patch $\boldsymbol{y}_{MS}$ to generate the vector $\boldsymbol{y}$. Then, the sparsity regularization (11) is resolved using the BP method to get the sparse representation $\hat{\boldsymbol{\alpha}}$ of the fused MS image patch. Finally, the fused MS image patch is obtained by $\hat{\boldsymbol{x}} = \mathbf{D}\hat{\boldsymbol{\alpha}}$.

B. Random Raw Patches Dictionary

The dictionary of sparse representation is a collection of parameterized waveforms called atoms [36]. The dictionary is overcomplete; in which case, the number of atoms of the dictionary exceeds the length of signal. In recent years, the sparsity-regularization-based image processing methods, such as denoising [31], [32], face recognition [33], and super-resolution [34], always lead to the state-of-the-art results.

In image processing applications, each column of the overcomplete dictionary $\mathbf{D}$ corresponds to an image or image patch in $\mathbf{R}^n$. Those images or image patches are referred as atomic images. A collection of parameterized 2-D waveforms of wavelets, Gabor dictionaries, and cosine packets is the commonly used dictionary [36]. Moreover, an application-orientated nonparametric dictionary may produce better result. However, dictionary learning is difficult and time-consuming. Simply, the dictionary can also be generated by randomly sampling raw patches from training images with similar statistical nature. The effectiveness of this kind of dictionary is validated in face recognition and image super-resolution application [33], [34]. In this paper, we generated the dictionary by randomly sampling raw patches from high-resolution MS satellite images. Because different satellite optical sensors have different characteristics in reflecting spectral information of scene, the high-resolution MS images with the same type of sensors should be used to construct the dictionary. When the sparse regularization is used, the proposed method selects a number of relevant dictionary elements adaptively for each patch. Thus, the reconstructed image can well preserve the spectral information of the scene. Our experiments in the following section also show the effectiveness of such dictionary.

In addition, based on the CS theory, correctly recovering signal $\boldsymbol{x}$ in (11) requires that the measurement matrix $\mathbf{M}$ is incoherent/uncorrelated to the dictionary $\mathbf{D}$. Because that the dictionary is generated by randomly sampling, it has the high probability satisfying this condition. Thus, for a variety of measurement matrix $\mathbf{M}$, any sufficiently sparse linear representation of $\boldsymbol{x}$ in terms of the dictionary $\mathbf{D}$ can be recovered almost perfectly from the high-resolution PAN and low-resolution MS images.

IV. Experimental Results and Comparisons

A. Quality Indices for Assessing Image Fusion

To evaluate different fusion methods, we need to check the synthesis property that any synthetic image should be as identical as possible to the image that the corresponding sensor would observe with the highest spatial resolution [37], [38]. So, Wald's protocol [37] is adopted, i.e., the fusion is performed on degraded data sets and the fused high-resolution MS images are then compared with the original low-resolution MS images which are seen as the reference images. In this paper, the following five typical evaluation metrics are used.

1) The correlation coefficient (CC) [39] is calculated by

$$\mathrm{CC} = \frac{\sum_{i=1}^{M}\sum_{j=1}^{N}\left[\boldsymbol{F}(i,j)-\bar{\boldsymbol{F}}\right]\left[\boldsymbol{X}(i,j)-\bar{\boldsymbol{X}}\right]}{\sqrt{\sum_{i=1}^{M}\sum_{j=1}^{N}\left[\boldsymbol{F}(i,j)-\bar{\boldsymbol{F}}\right]^2\sum_{i=1}^{M}\sum_{j=1}^{N}\left[\boldsymbol{X}(i,j)-\bar{\boldsymbol{X}}\right]^2}} \tag{12}$$

where $\boldsymbol{X}$ and $\boldsymbol{F}$ denote the source MS images and the fused image with size $M \times N$, respectively. The correlation coefficient indicates the degree of correlation between $\boldsymbol{X}$ and $\boldsymbol{F}$. When $\boldsymbol{F}$ equals to $\boldsymbol{X}$, the correlation coefficient approaches to one.

2) The spectral angle mapper (SAM) [39] reflects the spectral distortion by the absolute angles between the two vectors constructed from each pixel of the source image $\boldsymbol{X}$ and the fused image $\boldsymbol{F}$. Let $\boldsymbol{u}_X$ and $\boldsymbol{u}_F$ denote the spectral vector of a pixel of $\boldsymbol{X}$ and $\boldsymbol{F}$, respectively. The SAM is calculated by

$$\mathrm{SAM} = \arccos\left(\frac{\langle \boldsymbol{u}_X, \boldsymbol{u}_F\rangle}{\|\boldsymbol{u}_X\|_2 \cdot \|\boldsymbol{u}_F\|_2}\right). \tag{13}$$

The SAM is averaged over the whole image to yield a global measurement of spectral distortion. For ideal fused image, the SAM value should be zero.

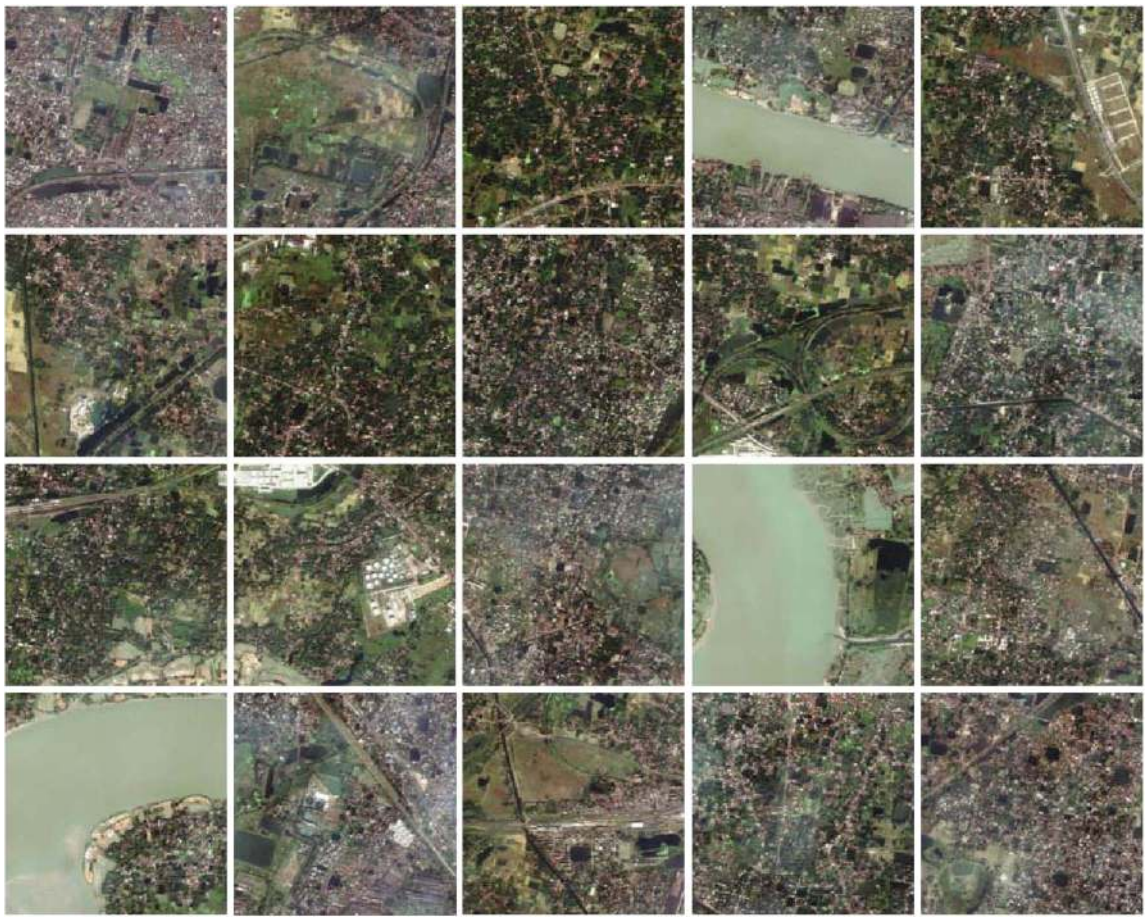

Fig. 4. Twenty satellite images used to construct dictionary.

3) The root mean squared error (RMSE) gives the standard measure of difference between two images. It is defined as

$$\text{RMSE} = \frac{1}{MN}\sqrt{\sum_{i,j=1}^{MN}(\boldsymbol{X}(i,j)-\boldsymbol{F}(i,j))^2}. \quad (14)$$

4) The *erreur relative global adimensionnelle de synthèse* (ERGAS) gives a global quality measure of the fused image $\boldsymbol{F}$ [38], which is defined as

$$\text{ERGAS} = 100\frac{h}{l}\sqrt{\frac{1}{P}\sum_{i=1}^{L}\left(\frac{\text{RMSE}^2(i)}{\text{MEAN}(i)}\right)} \quad (15)$$

where h is spatial resolution of the PAN image; l is spatial resolution of the MS images; P is the number of bands of the fused image $\boldsymbol{F}$; MEAN(i) is the mean value of the ith band of the reference MS images and RMSE(i) is the RMSE between the ith band of the reference MS images and the ith band of the fused image. Smaller ERGAS indicates better fusion result (ideally zero).

5) The Q4 index is defined as [40]

$$\text{Q4} = E(\text{Q4}_{D\times D}) \quad (16)$$

where $Q4_{D\times D}=\{4[E(x\cdot y^*)-\overline{x}\cdot\overline{y}^*]/(E(\|x\|^2)-\|\overline{x}\|^2+E(\|y\|^2)-\|\overline{y}\|^2)\}\cdot\{\|\overline{x}\|\cdot\|\overline{y}\|/(\|\overline{x}\|^2+\|\overline{y}\|^2)\}$. The quaternion $\boldsymbol{x} = X_1(m,n)+iX_2(m,n)+jX_3(m,n)+kX_4(m,n)$, $\boldsymbol{y} = F_1(m,n)+iF_2(m,n)+jF_3(m,n)+kF_4(m,n)$, F_i and X_i are the ith band of F and X, respectively. The $\boldsymbol{y}^*$ is the complex conjugate of $\boldsymbol{y}$, $\text{E}(\cdot)$ denotes the quaternion obtained by averaging the pixel quaternion within a D $\times$ D block with size of 8 $\times$ 8, and $\|\boldsymbol{x}\|$ is the modulus of $\boldsymbol{x}$. The Q4 index takes values in [0, 1] with one being the best value.

B. Fusion Results of QuickBird Data

QuickBird is a high-resolution satellite which provides PAN image at 0.7-m resolution and MS images at 2.8-m resolution. In order to evaluate the fusion results with objective measures, we spatially degrade the PAN and MS images with low-pass filter and decimation operator by four to yield one 2.8-m resolution PAN image and four 11.2- m resolution MS images. Then, the degraded low-resolution PAN and MS images are fused to produce one high-resolution MS image with 2.8-m resolution. The fused results are compared with the true 2.8-m MS image using the objective measures. The proposed method needs a dictionary which contains the raw image patches responding to 2.8-m resolution MS bands. In this paper, we randomly sample 10 000 raw patches from 20 images downloaded from the website http://glcf.umiacs.umd.edu/data/quickbird/. Empirically, we find that such dictionary can always produce very good fusion results. Fig. 4 shows 20 training images used

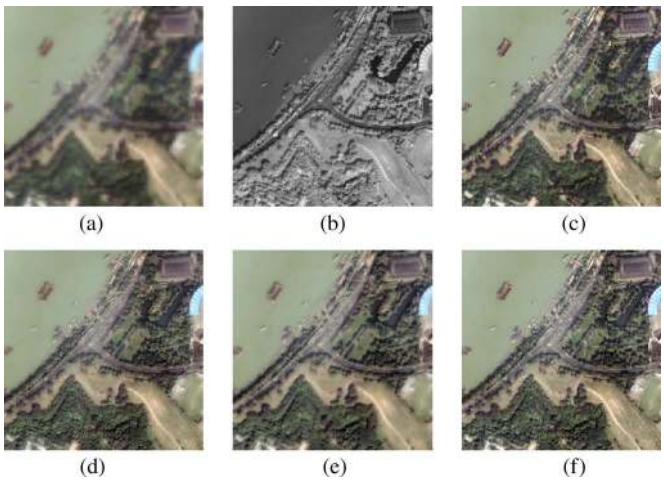

Fig. 5. Source QuickBird images (dock) and the fused results using different methods. (a) The resampled low-resolution MS image (RGB, 256 × 256, 11.2 m); (b) High-resolution PAN image (256 × 256, 2.8 m); (c) Original high-resolution MS image (RGB, 256 × 256, 2.8 m); (d) Fused RGB bands by SVT method; (e) Fused RGB bands by GA method; (f) Fused RGB bands by the proposed method.

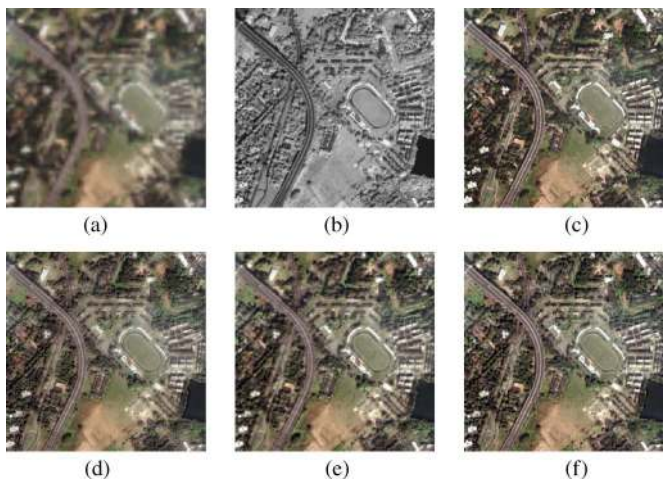

Fig. 6. Source QuickBird images (highway) and the fused results using different methods. (a) The resampled low-resolution MS image (RGB, 256 × 256, 11.2 m); (b) High-resolution PAN image (256 × 256, 2.8 m); (c) Original high-resolution MS image (RGB, 256 × 256, 2.8 m); (d) Fused RGB bands by SVT method; (e) Fused RGB bands by GA method; (f) Fused RGB bands by the proposed method.

to generate the dictionary. Here, only three color composites (bands 3–2–1) of the 2.8-m resolution MS data are reported.

One free parameter of the proposed method is ε, which restricts the reconstruction error. When the noise level of the source images is σ, we can directly set $\varepsilon = n(C\sigma)^2$. In our experience, the source images are all clear (standard deviation $\sigma = 0$), thus according to $\varepsilon = n(C\sigma)^2$, the parameter ε should be zero. However, as the value of ε decreases, the process of the BP becomes slower. In fact, in our experiments, the pan-sharpening quality is stable over a large range of ε, such as $\varepsilon \in [0, 5]$. Therefore, in order to ensure pan-sharpening quality as well as the computation efficiency of the proposed method, the parameter ε is set to be 1 in our experimental section. The experiments show that this ε gives good results for all the test cases. The weights in (9) are set from the QuickBird normalized spectral response as: $w_1 = 0.1139$ for the Blue band; $w_2 = 0.2315$ for the Green band; $w_3 = 0.2308$ for the Red band; and $w_4 = 0.4239$ for the NIR band [21]. In addition, we normalize columns of the dictionary as $\boldsymbol{d}_i/\|\boldsymbol{d}_i\|_2$, $i = 1, 2, \ldots, 10000$, so that the atoms in the dictionary have unit length.

The proposed method is compared with six commonly used pan-sharpening methods, namely, the generalized IHS (GIHS) [9], the GS transform [11], SVT [16], the ATWT-based method with the CBD injection model [19], the ATWT-based method with the AWLP model [17], and the ATWT-based method with the genetic algorithm (GA) [20]. Two levels of decompositions are used for the ATWT transform used for CBD, AWLP, and GA. In the case of SVT-based method, the σ^2 in the Gaussian RBF kernel is set to 1.2, and the parameter γ of the mapped LS-SVM is set to 1, which give the best results. The GS algorithm is implemented in the environment for visualizing images (ENVI) software [11], and we set that the low-resolution PAN image is simulated by averaging the low-resolution MS images.

Figs. 5(a) and (b) and 6(a) and (b) show two QuickBrid source images of the urban areas of Sundarbans, India, acquired on November 21, 2002. The original true 2.8-m RGB bands of the MS data are presented in Figs. 5(c) and 6(c) for visual reference. In order to save space, only the results of SVT- and GA-based methods and the proposed method are illustrated in Figs. 5(d)–(f) and 6(d)–(f), respectively. By visually comparing the fused images with the original source images, we can see that all the experimental methods can effectively pan-sharpen the MS data. However, compared to the original reference MS images, the pan-sharpened images with SVT- and GA-based methods are blurred in some degree. Careful inspections of Figs. 5(f) and 6(f) indicate that the proposed method not only provides high-quality spatial details but also preserves spectral information well. Particularly, the road in Fig. 6(f) is clearer than that in Fig. 6(d) and (e).

The objective measures for Figs. 5 and 6 are reported in Tables I and II, respectively, in which the best results for each quality measure are labeled in bold. The correlation coefficient (CC) allows us to determine the correlation between the pan-sharpened band and the original band in both spectral and spatial information. Both the tables show that the proposed approach provides the highest CC values for all the four bands. The root mean squared error (RMSE) measure gives radiometric distortion of the pan-sharpened band from the original MS data, while ERGAS offers a global depiction of the quality of radiometric distortion of the fused product. We can see that the proposed method only loses the NIR band for the RMSE. For the ERGAS, the proposed method also gives the best results. The SAM yields a global measurement of spectral distortion of the pan-sharpened images. Both the two tables show that the AWLP method gives the lowest SAM. We should note that, for other quality indexes, the proposed method performs obviously better than the AWLP method. Since the ERGAS only considers RMSE, and the SAM only considers spectral distortion, a more comprehensive measure of quality Q4 has been developed to test both spectral and spatial qualities of the fused images. For the Q4, the proposed method also provides the best results. This is mainly due to one advantage of the

TABLE I
COMPARISON OF THE PROPOSED ALGORITHM WITH THE EXISTING METHODS ON QUICKBIRD IMAGES SHOWN IN FIG. 5

		GIHS	GS	SVT	CBD	AWLP	GA	Our method
CC	R	0.7739	0.4803	0.9455	0.9365	0.9323	0.9420	**0.9535**
	G	0.8119	0.5165	0.9602	0.9503	0.9487	0.9567	**0.9636**
	B	0.6610	0.4913	0.9317	0.9249	0.9149	0.9392	**0.9572**
	N	0.9465	0.9451	0.9819	0.9710	0.9486	0.9733	**0.9829**
	avg	0.7983	0.6083	0.9548	0.9457	0.9361	0.9528	**0.9643**
RMSE	R	30.4373	41.7302	15.2079	17.1879	18.2282	15.6744	**14.3012**
	G	29.6553	41.6234	13.4734	15.8081	16.3486	14.0337	**13.1207**
	B	30.0960	34.9298	14.7340	16.1357	17.8095	13.7576	**11.6593**
	N	26.9072	17.4787	**10.1700**	13.5247	19.9397	12.2715	10.2056
	avg	29.2740	33.9405	13.3963	15.6641	18.0815	13.9343	**12.3217**
SAM		5.0993	8.1153	4.2298	4.3359	**3.3609**	4.2801	3.4447
ERGAS		6.3024	4.1053	2.3979	3.1766	4.6833	2.8820	**2.3970**
Q4		0.6852	0.5777	0.7728	0.7715	0.7500	0.7547	**0.8072**

TABLE II
COMPARISON OF THE PROPOSED ALGORITHM WITH THE EXISTING METHODS ON QUICKBIRD IMAGES SHOWN IN FIG. 6

		GIHS	GS	SVT	CBD	AWLP	GA	Our method
CC	R	0.8218	0.7254	0.9051	0.8932	0.8942	0.8856	**0.9206**
	G	0.8148	0.7381	0.9112	0.8996	0.9057	0.9010	**0.9227**
	B	0.7318	0.7186	0.8734	0.8623	0.8744	0.8688	**0.9127**
	N	0.8793	0.9041	0.9440	0.9259	0.8982	0.9418	**0.9509**
	avg	0.8119	0.7716	0.9084	0.8953	0.8931	0.8993	**0.9276**
RMSE	R	29.7992	34.9509	21.6018	23.9296	24.2942	23.7347	**20.0787**
	G	28.5333	32.5814	19.9279	22.2514	21.6641	20.9869	**18.9361**
	B	28.5636	29.1218	20.4475	22.8862	21.7609	20.8525	**17.1369**
	N	22.3728	17.2943	**13.3277**	17.4710	25.9061	13.6543	13.3955
	avg	27.3172	28.4871	18.8262	21.6345	23.4063	19.8071	**17.3868**
SAM		6.3150	8.0417	6.3809	6.8568	**5.0841**	6.3785	5.5341
ERGAS		4.2372	3.2744	2.5426	3.3078	4.9049	2.5842	**2.5362**
Q4		0.7150	0.6678	0.8192	0.8166	0.8074	0.8002	**0.8609**

proposed scheme over other comparing methods that it selects atom patches from the dictionary adaptively for each patch. Those patches are the most relevant ones in the dictionary to represent the given low-resolution MS images and the PAN image because of the sparsity regularization in (11). Thus, the reconstructed high-resolution MS images from the selected patches can preserve well both spatial and spectral information of the source images.

C. Fusion Results of IKONOS Data

In this section, we describe and analyze the experimental results on the IKONOS satellite data. The IKONOS satellite captures 4-m MS images, i.e., blue, green, red, and NIR images, and 1-m PAN image. As the QuickBrid experiment, we spatially degrade the IKONOS images with decimation by four to yield 4-m PAN and 16-m MS images. Then, the degraded images are fused to produce 4-m MS images. The fusion results are compared with the true 4-m MS image to achieve the objective measures. The dictionary, which contains the 10 000 raw image patches, is randomly sampled from 20 training images obtained from the website http://glcf.umiacs.umd.edu/data/ikonos/index.shtml. For IKONOS fusion, the weights in (10) are set the same as those for QuickBird data since the spectral response of IKONOS is very similar to QuickBird, and other experimental settings are also the same as those for QuickBrid case.

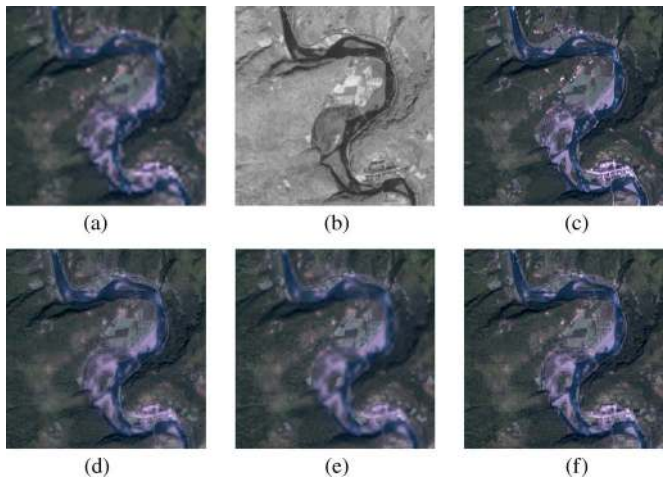

Fig. 7. Source IKONOS images (river area) and the fused results using different methods. (a) The resampled low-resolution MS image (RGB, 256 × 256, 16 m); (b) High-resolution PAN image (256 × 256, 4 m); (c) Original high-resolution MS image (RGB, 256 × 256, 4 m); (d) Fused RGB bands by SVT method; (e) Fused RGB bands by GA method; (f) Fused RGB bands by the proposed method.

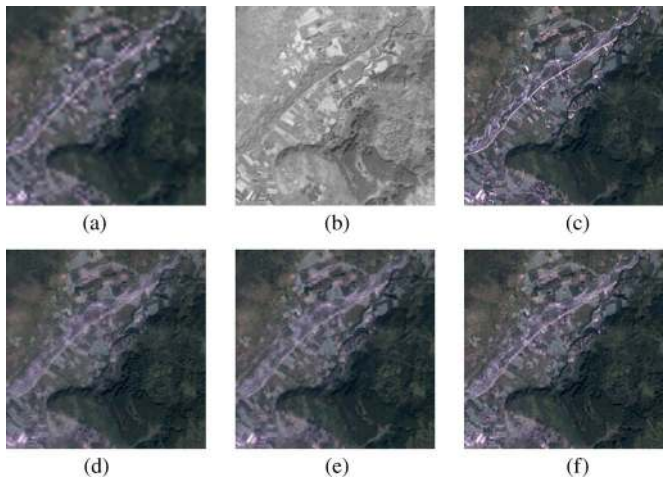

Fig. 8. Source IKONOS images (rural area) and the fused results using different methods. (a) The resampled low-resolution MS image (RGB, 256 × 256, 16 m); (b) High-resolution PAN image (256 × 256, 4 m); (c) Original high-resolution MS image (RGB, 256 × 256, 4 m); (d) Fused RGB bands by SVT method; (e) Fused RGB bands by GA method; (f) Fused RGB bands by the proposed method.

Fig. 7(a) shows a resampled low-resolution IKONOS MS image of one region in Sichuan, China, acquired on May 15, 2008. Fig. 7(b) gives the corresponding degraded IKONOS high-resolution PAN image. The true high-resolution 4-m MS image is presented in Fig. 7(c). Comparing Fig. 7(b) with Fig. 7(c), it can be found that the details of the PAN image are not as rich as those of the MS image. For example, the river beach area in the PAN image is darker than the area of the MS image. These features make this figure be difficult for pan-sharpening. Fig. 7(d)–(f) illustrate the results of different fusion methods. As shown in Fig. 7(d), the SVT provides the fused image with well-preserved spatial and spectral details. The fused image with the GA-based method preserves spectral

TABLE III
COMPARISON OF THE PROPOSED ALGORITHM WITH THE EXISTING METHODS ON IKONOS IMAGES SHOWN IN FIG. 7

		GIHS	GS	SVT	CBD	AWLP	GA	Our method
CC	R	0.6996	0.5373	0.8737	0.8660	0.8698	0.8667	**0.8800**
	G	0.5407	0.5375	0.8621	0.8529	0.8373	0.8734	**0.8797**
	B	0.7327	0.7216	0.8897	0.8852	0.8458	0.8810	**0.9087**
	N	0.9001	0.9213	0.9318	0.9199	0.8986	0.9351	**0.9376**
	avg	0.7183	0.6794	0.8893	0.8810	0.8629	0.8891	**0.9015**
RMSE	R	23.8032	28.1669	16.1182	16.9032	16.6188	16.5297	**15.8672**
	G	21.6039	21.5659	12.9343	13.8735	15.0928	12.3736	**12.2191**
	B	22.8489	23.8367	14.8680	15.4188	18.7340	15.4191	**13.6310**
	N	20.8977	17.1384	14.6026	16.1876	18.6312	14.2611	**14.1367**
	avg	22.2884	22.6770	14.6308	15.5958	17.2692	14.6459	**13.9635**
SAM		4.7430	5.9767	4.4521	4.6684	**3.9930**	4.6354	4.2370
ERGAS		5.2853	4.3346	3.6932	4.0941	4.7121	3.6068	**3.5754**
Q4		0.5694	0.5660	0.6873	0.7024	0.6686	0.6805	**0.7444**

TABLE IV
COMPARISON OF THE PROPOSED ALGORITHM WITH THE EXISTING METHODS ON IKONOS IMAGES SHOWN IN FIG. 8

		GIHS	GS	SVT	CBD	AWLP	GA	Our method
CC	R	0.7657	0.6690	0.8819	0.8752	0.8794	0.8748	**0.8881**
	G	0.6886	0.6818	0.8825	0.8724	0.8681	0.8892	**0.8973**
	B	0.7441	0.6795	0.8890	0.8840	0.8675	0.8850	**0.9068**
	N	0.8088	0.8580	0.8614	0.8495	0.8137	0.8728	**0.8823**
	avg	0.7518	0.7221	0.8787	0.8703	0.8572	0.8805	**0.8936**
RMSE	R	24.8748	28.8609	18.2064	18.8741	18.5000	18.7521	**17.8892**
	G	22.1292	22.3801	14.2709	15.2394	15.5797	13.8678	**13.4660**
	B	23.4237	25.7602	16.0592	16.6131	18.0016	16.3791	**14.8257**
	N	21.6651	16.0974	15.5132	16.8012	20.2409	14.9161	**14.5196**
	avg	23.0232	23.2746	16.0124	16.8820	18.0805	15.9788	**15.1751**
SAM		4.9192	6.2837	4.6762	4.5826	**4.0316**	4.6734	4.3178
ERGAS		4.8788	3.6250	3.4934	3.7835	4.5580	3.3589	**3.2697**
Q4		0.5813	0.5330	0.6618	0.6860	0.6589	0.6657	**0.7248**

details well. However, the spatial details in the river area are lost. The fused image obtained by the proposed CS-based approach preserves both spectral and spatial detailed information well. In particular, one can see that the details in the mountain areas and the river area are sharply increased. Fig. 8 shows another IKONOS image of one region in Sichuan, China. The similar conclusions can be drawn from Fig. 8.

The objective measures of the fused images in Figs. 7 and 8 are listed in Tables III and IV, respectively. From Table III, we can see that the proposed method performs the best in term of measures CC, RMSE, ERGAS, and Q4. The AWLP method provides the best value of SAM followed by the proposed method. However, for other quality indexes, the proposed method performs better than the AWLP. Therefore, on the whole, the proposed method provides the best fused results. For the Table IV, the proposed method only loses the SAM quality index. The proposed method performs the best for other measures.

V. CONCLUSION

In this paper, a novel pan-sharpening method based on CS technique is presented. Based on the PAN and MS images generation model, we referred the pan-sharpening problem as an ill-posed inverse problem inherently. Then, the sparsity regularization is employed to address the ill-posed inverse problem, and the high-resolution spectral image can be effectively recovered. The proposed method is tested on QuickBird and IKONOS images and compared with six well-known methods: 1) GIHS; 2) GS; 3) SVT; 4) CBD; 5) AWLP; and 6) GA-based methods. The spectral and spatial information are comprehensively evaluated using several image quality measures. The experimental results demonstrate the effectiveness of sparsity as a prior for satellite PAN and MS image fusion. In addition, we notice that the proposed method can easily process image fusion and restoration when the source images are corrupted by noise by only adjusting the parameter ε in (11).

However, the proposed scheme takes more time than traditional methods. In the future, we can implement the proposed fusion scheme paralleled on multicore processors, because the time-consuming BP can be done independently on each patch. And, we should note that, in much imaging situations, the images may be contaminated by other types of noise, such as the Poisson noise in low-light-level images. Thus, the setting of parameter ε or even the optimal function (11) need to be further studied. For simplicity, only the Gaussian noise is considered in this paper. In addition, readers should note that the linear relationship used in this paper is only an approximate model. It is feasible for QuickBird and IKONOS satellites, but need to be modified when applying to other space missions or other modalities.

ACKNOWLEDGMENT

The authors would like to thank the anonymous reviewers for their detailed review, valuable comments, and constructive suggestions.

REFERENCES

[1] L. Wald, "Some terms of reference in data fusion," *IEEE Trans. Geosci. Remote Sens.*, vol. 37, no. 3, pp. 1190–1193, May 1999.
[2] C. Thomas, T. Ranchin, L. Wald, and J. Chanussot, "Synthesis of multispectral images to high spatial resolution: A critical review of fusion methods based on remote sensing physics," *IEEE Trans. Geosci. Remote Sens.*, vol. 46, no. 5, pp. 1301–1312, May 2008.
[3] B. Aiazzi, S. Baronti, and M. Selva, "Improving component substitution pan-sharpening through multivariate regression of MS +Pan data," *IEEE Trans. Geosci. Remote Sens.*, vol. 45, no. 10, pp. 3230–3239, Oct. 2007.
[4] J. Lee and C. Lee, "Fast and efficient panchromatic sharpening," *IEEE Trans. Geosci. Remote Sens.*, vol. 48, no. 1, pp. 155–163, Jan. 2010.
[5] M. González-Audícana, X. Otazu, O. Fors, and J. Alvarez-Mozos, "A low computational-cost method to fuse IKONOS images using the spectral response function of its sensors," *IEEE Trans. Geosci. Remote Sens.*, vol. 44, no. 6, pp. 1683–1691, Jun. 2006.
[6] P. S. Pradhan, R. L. King, N. H. Younan, and D. W. Holcomb, "Estimation of the number of decomposition levels for a wavelet-based multiresolution multisensor image fusion," *IEEE Trans. Geosci. Remote Sens.*, vol. 44, no. 12, pp. 3674–3686, Dec. 2006.
[7] V. Buntilov and T. R. Bretschneider, "A content separation image fusion approach: Toward conformity between spectral and spatial information," *IEEE Trans. Geosci. Remote Sens.*, vol. 45, no. 10, pp. 3252–3263, Oct. 2007.
[8] M. Choi, "A new intensity-hue-saturation fusion approach to image fusion with a tradeoff parameter," *IEEE Trans. Geosci. Remote Sens.*, vol. 44, no. 6, pp. 1672–1682, Jun. 2006.
[9] T.-M. Tu, P. S. Huang, C.-L. Hung, and C.-P. Chang, "A fast intensity-hue-saturation fusion technique with spectral adjustment for IKONOS imagery," *IEEE Geosci. Remote Sens. Lett.*, vol. 1, no. 4, pp. 309–312, Oct. 2004.
[10] P. S. Chavez, S. C. Sides, and J. A. Anderson, "Comparison of three different methods to merge multiresolution and multispectral data: Landsat

TM and SPOT panchromatic," *Photogramm. Eng. Remote Sens.*, vol. 57, no. 3, pp. 295–303, Mar. 1991.
[11] C. A. Laben and B. V. Brower, "Process for enhancing the spatial resolution of multispectral imagery using pan-sharpening," U.S. Patent 6 011 875, Jan. 4, 2000, Tech. Rep., Eastman Kodak Company.
[12] T. Ranchin and L. Wald, "Fusion of high spatial and spectral resolution images: The ARSIS concept and its implementation," *Photogramm. Eng. Remote Sens.*, vol. 66, no. 1, pp. 49–61, Jan. 2000.
[13] T. Ranchin, B. Aiazzi, L. Alparone, S. Baronti, and L. Wald, "Image fusion. The ARSIS concept and some successful implementation schemes," *ISPRS J. Photogramm. Remote Sens.*, vol. 58, no. 1/2, pp. 4–18, Jun. 2003.
[14] J. Núñez, X. Otazu, O. Fors, A. Prades, V. Palà, and R. Arbiol, "Multiresolution-based image fusion with additive wavelet decomposition," *IEEE Trans. Geosci. Remote Sens.*, vol. 37, no. 3, pp. 1204–1211, May 1999.
[15] V. P. Shah, N. H. Younan, and R. L. King, "An efficient pan-sharpening method via a combined adaptive PCA approach and contourlets," *IEEE Trans. Geosci. Remote Sens.*, vol. 46, no. 5, pp. 1323–1335, May 2008.
[16] S. Zheng, W. Z. Shi, J. Liu, and J. W. Tian, "Remote sensing image fusion using multiscale mapped LS-SVM," *IEEE Trans. Geosci. Remote Sens.*, vol. 46, no. 5, pp. 1313–1322, May 2008.
[17] X. Otazu, M. González-Audícana, O. Fors, and J. Núñez, "Introduction of sensor spectral response into image fusion methods. Application to wavelet-based methods," *IEEE Trans. Geosci. Remote Sens.*, vol. 43, no. 10, pp. 2376–2385, Oct. 2005.
[18] B. Aiazzi, L. Alparone, S. Baronti, and A. Garzelli, "Context-driven fusion of high spatial and spectral resolution images based on oversampled multiresolution analysis," *IEEE Trans. Geosci. Remote Sens.*, vol. 40, no. 10, pp. 2300–2312, Oct. 2002.
[19] A. Garzelli and F. Nencini, "Interband structure modeling for pan-sharpening of very high-resolution multispectral images," *Inf. Fusion*, vol. 6, no. 3, pp. 213–224, Sep. 2005.
[20] A. Garzelli and F. Nencini, "PAN-sharpening of very high resolution multispectral images using genetic algorithms," *Int. J. Remote Sens.*, vol. 27, no. 15, pp. 3273–3292, Aug. 2006.
[21] M. V. Joshi, L. Bruzzone, and S. Chaudhuri, "A model-based approach to multiresolution fusion in remotely sensed images," *IEEE Trans. Geosci. Remote Sens.*, vol. 44, no. 9, pp. 2549–2562, Sep. 2006.
[22] A. Garzelli, F. Nencini, and L. Capobianco, "Optimal MMSE pan sharpening of very high resolution multispectral images," *IEEE Trans. Geosci. Remote Sens.*, vol. 46, no. 1, pp. 228–236, Jan. 2008.
[23] Z. H. Li and H. Leung, "Fusion of multispectral and panchromatic images using a restoration-based method," *IEEE Trans. Geosci. Remote Sens.*, vol. 47, no. 5, pp. 1482–1491, May 2009.
[24] K. A. Kalpoma and J. I. Kudoh, "Image fusion processing for IKONOS 1-m color imagery," *IEEE Trans. Geosci. Remote Sens.*, vol. 45, no. 10, pp. 3075–3086, Oct. 2007.
[25] D. Fasbender, J. Radoux, and P. Bogaert, "Bayesian data fusion for adaptable image pansharpening," *IEEE Trans. Geosci. Remote Sens.*, vol. 46, no. 6, pp. 1847–1857, Jun. 2008.
[26] Y. F. Zhang, S. D. Backer, and P. Scheunders, "Noise-resistant wavelet-based Bayesian fusion of multispectral and hyperspectral images," *IEEE Trans. Geosci. Remote Sens.*, vol. 47, no. 11, pp. 3834–3843, Nov. 2009.
[27] M. Joshi and A. Jalobeanu, "MAP estimation for multiresolution fusion in remotely sensed images using an IGMRF prior model," *IEEE Trans. Geosci. Remote Sens.*, vol. 48, no. 3, pp. 1245–1255, Mar. 2010.
[28] D. L. Donoho, "Compressed sensing," *IEEE Trans. Inf. Theory*, vol. 52, no. 4, pp. 1289–1306, Apr. 2006.
[29] E. Candès, J. Romberg, and T. Tao, "Stable signal recovery from incomplete and inaccurate information," *Commun. Pure Appl. Math.*, vol. 59, no. 8, pp. 1207–1233, Feb. 2005.
[30] M. Elad, M. A. T. Figueiredo, and Y. Ma, "On the role of sparse and redundant representations in image processing," *Proc. IEEE*, vol. 98, no. 6, pp. 972–982, Jun. 2010.
[31] J. Mairal, M. Elad, and G. Sapiro, "Sparse representation for color image restoration," *IEEE Trans. Image Process.*, vol. 17, no. 1, pp. 53–69, Jan. 2008.
[32] M. Elad and M. Aharon, "Image denoising via sparse and redundant representations over learned dictionaries," *IEEE Trans. Image Process.*, vol. 15, no. 12, pp. 3736–3745, Dec. 2006.
[33] J. Wright, A. Y. Yang, A. Ganesh, S. S. Sastry, and Y. Ma, "Robust face recognition via sparse representation," *IEEE Trans. Pattern Anal. Mach. Intell.*, vol. 31, no. 2, pp. 210–227, Feb. 2009.
[34] J. C. Yang, J. Wright, Y. Ma, and T. Huang, "Image super-resolution as sparse representation of raw image patches," in *Proc. IEEE Int. Conf. Comput. Vis. Pattern Recog.*, Anchorage, AK, Jun. 2008, pp. 1–8.
[35] D. Donoho, "For most large underdetermined systems of linear equations the minimal l_1-norm near solution approximates the sparsest solution," *Commun. Pure Appl. Math.*, vol. 59, no. 10, pp. 907–934, Jul. 2006.
[36] S. Chen, D. Donoho, and M. Saunders, "Atomic decomposition by basis pursuit," *SIAM Rev.*, vol. 43, no. 1, pp. 129–159, 2001.
[37] L. Wald, T. Ranchin, and M. Mangolini, "Fusion of satellite images of different spatial resolutions: Assessing the quality of resulting images," *Photogramm. Eng. Remote Sens.*, vol. 63, no. 6, pp. 691–699, Jun. 1997.
[38] M. M. Khan, L. Alparone, and J. Chanussot, "Pansharpening quality assessment using the modulation transfer functions of instruments," *IEEE Trans. Geosci. Remote Sens.*, vol. 47, no. 11, pp. 3880–3891, Nov. 2009.
[39] L. Alparone, L. Wald, J. Chanussot, C. Thomas, P. Gamba, and L. M. Bruce, "Comparison of pansharpening algorithms: Outcome of the 2006 GRS-S data-fusion contest," *IEEE Trans. Geosci. Remote Sens.*, vol. 45, no. 10, pp. 3012–3021, Oct. 2007.
[40] L. Alparone, S. Baronti, A. Garzelli, and F. Nencini, "A global quality measurement of pan-sharpened multispectral imagery," *IEEE Geosci. Remote Sens. Lett.*, vol. 1, no. 4, pp. 313–317, Oct. 2004.

Shutao Li (M'07) received the B.S., M.S., and Ph.D. degrees in electrical engineering from Hunan University, Changsha, China, in 1995, 1997, and 2001, respectively.

From May 2001 to October 2001, he was a Research Associate with the Department of Computer Science, Hong Kong University of Science and Technology, Clear Water Bay, NT, Hong Kong. From November 2002 to November 2003, he was a Postdoctoral Fellow with the Royal Holloway College, University of London, Egham, U.K. From April 2005 to June 2005, he was a Visiting Professor with the Department of Computer Science, Hong Kong University of Science and Technology. He is currently a Full Professor with the College of Electrical and Information Engineering, Hunan University. He has authored or coauthored more than 100 refereed papers. His professional interests are information fusion, pattern recognition, computational intelligence, and image processing.

Dr. Li has won two Second-Grade National Awards at the Science and Technology Progress of China in 2004 and 2006

Bin Yang received the B.S. degree from Zhengzhou University of Light Industry, Zhengzhou, China, in 2005. He is currently working toward the Ph.D. degree in Hunan University, Changsha, China.

His technical interests include image fusion and pattern recognition.